CHINESE OPTICS LETTERS

Vol. 20, No. 4 | April 2022

Single-frequency Er:YAG ceramic pulsed laser with frequency stability close to 100 kHz

Chaoyong Chen (陈朝勇)[1,2], Chunqing Gao (高春清)[1,2*], Huixing Dai (戴会星)[1,2], and Qing Wang (王 庆)[1,2]

[1] School of Optics and Photonics, Beijing Institute of Technology, Beijing 100081, China

[2] Key Laboratory of Information Technology, Ministry of Industry and Information Technology, Beijing 100081, China

*Corresponding author: gao@bit.edu.cn

Received December 6, 2021 | Accepted January 19, 2022 | Posted Online February 11, 2022

A single-frequency 1645 nm pulsed laser with frequency stability close to 100 kHz was demonstrated. The laser oscillator is injection-seeded by a single-frequency narrow linewidth Er:$Y_3Al_5O_{12}$ (Er:YAG) nonplanar ring oscillator and frequency stabilized by the modified Pound–Drever–Hall method. The pulse repetition rate can be set from 100 to 500 Hz with the frequency stability from 82.72 kHz to 134.44 kHz and pulse energy from 9.84 mJ to 19.55 mJ. To our knowledge, this is the best frequency stability of a single-frequency pulsed laser with injection-seeding.

Keywords: single-frequency pulse; high-frequency stability; injection-seeding.

DOI: 10.3788/COL202220.041402

1. Introduction

Frequency stabilization of remote coherent Doppler lidar or differential absorption lidar laser transmitters is essential for obtaining a high accuracy and a high signal-to-noise ratio (SNR)[1–7], especially for space-based lidars[8–13]. Injection-seeding to a *Q*-switched laser is a powerful way for these remote lidar applications. General methods to establish the single-frequency operation of the injection-seeding *Q*-switched configuration are minimizing the *Q*-switch build time[14], ramp-fire (or ramp-hold-fire)[15,16], dither lock-in[17], the Pound–Drever–Hall (PDH) method[1], and so on. Among them, the PDH technique may be the best way to improve the frequency stability of the single-frequency pulses for the following reasons.

(1) It can keep the cavity length in a relatively stable state, which means that the slave cavity is resonant with the seed beam almost all of the time.
(2) The 'ramp' or 'dither' operation is not required in the interval between pulses. It keeps the slave cavity in a relatively 'quiet' environment.
(3) The pulse intervals obtained by the PDH method are strictly consistent, which are controlled by an external transistor-transistor logic (TTL) signal source.
(4) It holds the seed beam resonant with one definite longitudinal mode of the slave cavity, and the mode hopping can be avoided.

The PDH method was first, to the best of our knowledge, introduced in the pulse domain by Wulfmeyer in 2000, and a short-term frequency stability of 0.18 MHz root mean square (rms) at pulse repetition rate (PRR) of 200 Hz was reported[1]. In 2007, Sträßer *et al.* applied the PDH method to an injection-seeded Nd:$Y_3Al_5O_{12}$ (Nd:YAG) ring oscillator and achieved frequency stability of 1 MHz rms at the PRR of 400 Hz[18], and they improved the frequency stability to 290 kHz in 2009[19]. In 2014 and 2015, Gibert *et al.* reported a two-wavelength single-frequency Ho:$YLiF_4$ (Ho:YLF) laser oscillator with the frequency stability of 2.6 MHz at a repetition of 2 kHz and its application in a differential absorption lidar for the detection of CO_2 in the atmosphere[9,20]. In 2020, we reported 10.31 mJ single-frequency pulses with optimal frequency stability of 525 kHz at the PRR of 1 kHz[21].

In this paper, we demonstrated that the frequency instability of the single-frequency pulses can be controlled close to 100 kHz by following the PDH scheme. Compared with our previous work, we optimized the laser resonance cavity, the mechanical structure, and the feedback control system. The PRR can be set from 100 to 500 Hz with hundreds of nanoseconds pulse duration, the frequency stability varies from 82.72 kHz to 134.44 kHz and pulse energy from 9.84 mJ to 19.55 mJ. The beam quality M^2 factors of the output laser are 1.24 in the *X* direction and 1.21 in the *Y* direction, respectively. Besides, we analyzed the influence of pulse frequency stability on the SNR and measurement accuracy of the remote coherent Doppler lidar by means of numerical simulation, and the Allan variance of the frequency stability was also given.

2. Analysis

For the remote coherent Doppler lidar or differential absorption lidar, pulse accumulation or averaging is a very practical method

to improve the detection accuracy and range. Here, we take the coherent Doppler wind lidar as an example and analyze the influence of pulse frequency stability on SNR and measurement accuracy of the lidar echo in detail by means of the numerical simulation.

The echo signal of the Doppler lidar is the superposition of a large number of aerosol particles' backscattered signals, and the phase of the backscattered signal of each particle is randomly distributed, so the Doppler signal can be described by a zero-mean complex Gaussian process. According to Zrnic's theory of weather Doppler signal simulation[22], the Doppler signal model z_k can be written as

$$z_k = s_k \exp(j2\pi f k T_s) + n_k, \tag{1}$$

where f is the Doppler shift, and T_s is the sampling interval. The stationary random signal s_k and the uncorrelated noise n_k are independent of each other. The relationship between the power spectral density P_m and covariance R_k of the Doppler signal is as follows[23]:

$$P_m = \frac{1}{2M} \sum_{k=0}^{2M-1} R_k \exp\left(-\frac{\pi i m k}{M}\right), \tag{2}$$

$$R_k = \mathrm{SNR}_{\mathrm{sp}} \exp\left[-2(\pi \Delta\omega T_s k)^2 + j4\pi \nu T_s \frac{k}{\lambda}\right] + \delta_k, \tag{3}$$

where

$$\Delta\omega = \sqrt{\ln 2}/\left(\sqrt{2}\pi \Delta T\right) \tag{4}$$

is the spectral width of the echo signal, M is the number of sampling points, $\mathrm{SNR}_{\mathrm{sp}}$ is the SNR of one pulse, ΔT is the pulse width, $\nu = 2f/\lambda$ is the radial wind velocity, λ is the laser wavelength, and δ_k is the Kronecker delta function. The power spectral density P_m satisfies the following formula:

$$\langle p_k \cdot p_m^* \rangle = P_m \delta_{k-m}, \qquad |p_m|^2 = P_m, \tag{5}$$

where p_m is also a zero-mean complex Gaussian random variable. The simulated lidar echo signal is as follows:

$$z_k = \sum_{m=0}^{2M-1} p_m \exp\left(\frac{imk\pi}{M}\right). \tag{6}$$

In order to simplify the simulation, we consider that only white noise affects the echo signal. The frequency jitter Δf of each pulse is added to the Doppler shift. The frequency jitters are normally distributed. In order to visually see the impact of the pulse frequency stability on the SNR and measurement accuracy, we selected the standard deviation of frequency jitter as 0.5 MHz, 1 MHz, 5 MHz, and 10 MHz, and the relative power spectra of the echo signal are shown in Fig. 1.

As shown in Fig. 1, the pulse frequency jitter has a great influence on the SNR after the pulse accumulation. The higher the stability of pulse frequency is, the higher the SNR of the Doppler lidar is. Another obvious feature is that the smaller the pulse frequency jitter, the narrower the spectral width of the Doppler signal and the sharper the peak value, which means the higher the accuracy of speed measurement.

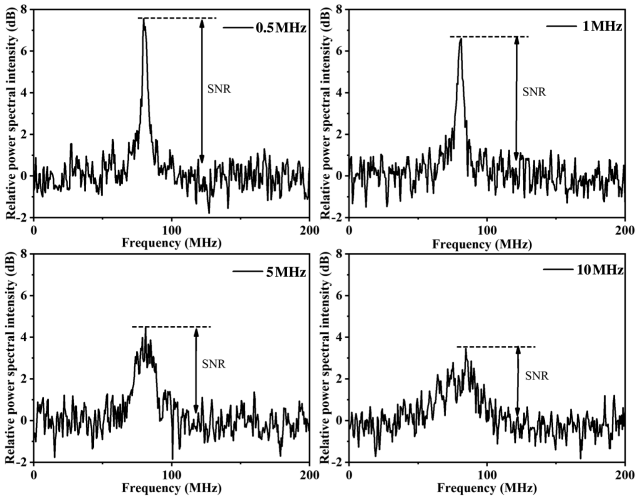

Fig. 1. Simulation of the Doppler lidar echo signals' relative power spectrum data with pulse frequency stability of 0.5 MHz, 1 MHz, 5 MHz, and 10 MHz. The lidar emits Gaussian pulses with the wavelength of λ = 1645 nm, $\mathrm{SNR}_{\mathrm{sp}}$ = -10 dB, f = 80 MHz, $1/T_s$ = 500 MHz, ΔT = 200 ns, and the cumulative number of pulses is 100.

3. Experimental Setup

The schematic diagram of our injection-seeded single-frequency Er:YAG laser is shown in Fig. 2. It consists of three main parts: a continuous wave seed laser, a Q-switched slave ring cavity, and an injection-seeding control system.

A symmetrical and compact slave ring cavity, which is composed with eight cavity mirrors (from M1 to M8), is adopted in our experiment for improving the stability and the beam quality. The designed total cavity length is about 2.2 m for meeting the requirements of the remote coherent Doppler lidar regarding pulse width. M1, M2, M7, and M8 are dichroic mirrors with a transmittance of more than 95% at 1470 nm and a reflectance of more than 99.5% at 1645 nm. Both M3 and M5 are plano-concave mirrors with a radius of curvature of 1000 mm. The difference is that M3 is an output mirror with a transmittance of 20% at 1645 nm, while M5 is a high-reflection mirror at 1645 nm. M4 and M5 are plane high-reflection mirrors at 1645 nm. Unlike our previous designs, the piezoelectric transducer (PZT) and mirror M4 are pressed together by a mechanical structure rather than glued together, with a rubber ring between them. Then, a pre-stressing force is applied to the PZT. This method effectively avoids the reduction of the PZT mechanical resonance frequency caused by gluing, and it ensures that the PZT can not only push M4 to change the cavity length but also maintain sufficient response bandwidth. Two

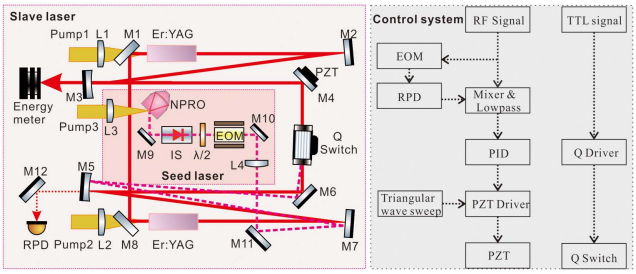

Fig. 2. Experimental setup of a frequency stabilized, *Q*-switched 1645 nm ceramic Er:YAG laser based on the PDH method. NPRO, nonplanar ring oscillator seed laser; HWP, half-wave plate; EOM, electro-optic phase modulator; AOM, acousto-optic *Q*-switch; PZT, piezoelectric transducer; PID, proportional-integral-differential controller; RPD, resonant photo-detector.

continuous wave 1470 nm fiber coupled diode lasers (Pump 1 and Pump 2) pump two 0.25% (atomic fraction) doped, ϕ4 mm × 60 mm Er:YAG ceramic rods. The fiber core diameters are 200 μm, and the numerical apertures are 0.22. The pump beams are mode matched with the slave cavity by two pairs of lenses with the focal lengths of 30 mm and 125 mm, respectively. The radii of the pumping beams in the Er:YAG rods center are about 420 μm, which are about 0.95 times the radius of the laser beams within the crystals. The Er:YAG rods are encased in a copper heat sink and temperature controlled by thermal electric coolers (TECs) to 18°C.

The single-frequency seed laser is generated by a 1470 nm laser diode pumped monolithic Er:YAG crystal nonplanar ring oscillator (NPRO) with a linewidth of 8 kHz[24]. The seed laser is sideband modulated by an electro-optical phase modulator (EOM) with a modulation frequency of 30 MHz. The half-wave plate keeps the polarization direction of the seed laser consistent with the optic axis of the EOM for the best modulation effect. The seed laser is reflected by M11, M7, M5, and M6 and then enters the slave ring cavity from the first diffraction stage of the acousto-optic *Q*-switch (AOM). The driver power of the AOM is 50 W with a radio frequency (RF) of 40.68 MHz. An isolator with isolation greater than 30 dB is placed on the seed light path to prevent laser feedback to the NPRO.

The control system and control process of our experimental setup are shown in Fig. 2(b). Firstly, a triangular wave sweep signal with a frequency of 100 Hz is loaded onto the PZT via the PZT driver. At this time, the cavity length of the slave resonant cavity is periodically modulated. M10, L4, and M11 are fine-tuned to match the pattern of the seed laser and the slave cavity. If the patterns matches well, the DC terminal of the resonant photo-detector (RPD) will output a periodic, smooth resonance signal[25]. Secondly, RF signals are applied with the same frequency but different phases to the EOM and the mixer, one of which is used to modulate the seed light, and the other is used to demodulate the detuned signal obtained by the AC terminal of the RPD, that is, the error signal. Thirdly, the center of the error signal is adjusted to zero by a bias voltage, and then the PZT driving voltage is slowly changed to change the PZT position until the length of the slave cavity matches the wavelength of the seed light. Fourthly, the proportional-integral- differential (PID) controller is turned on. If the PID parameter is appropriate, the length of the driven cavity will match the wavelength of the seed light, that is, the resonant signal will always stay at the highest value. Finally, the TTL signal for *Q*-switching is applied to the *Q* driver. Different from our previous design, a serial analog PID circuit is adopted, which has lower noise and higher low-frequency gain. A notch filter and a low-pass filter are added to the PID circuit to suppress the mechanical resonance of the PZT, which makes it possible to improve the stability of the control system by further increasing the low-frequency gain of the control loop.

What is more, the laser is encapsulated in a sealed aluminum shell to isolate external vibrations such as sound, air flow, and human activities.

4. Results and Discussion

When the pump power was 72 W, the free-running slave cavity laser produced a bidirectional 1645 nm continuous wave laser output of up to 6.4 W, which was tested by a power meter (PM100D/S314C, Thorlabs). At the injection-seeding operation, the average energies of the single-frequency pulses were 19.55 mJ, 16.99 mJ, 13.67 mJ, 11.19 mJ, and 9.84 mJ at PRRs of 100 Hz, 200 Hz, 300 Hz, 400 Hz, and 500 Hz, respectively. The energy of each pulse was measured by an energy meter (1919-R, Newport), and 10,000 pulses were recorded at each PRR, as shown in Fig. 3. According to the statistical results, the relative energy instability of pulses is approximately 0.5%, which shows that the pulse energy has good stability.

By performing coherent heterodyning of the seed laser and pulsed laser, we verified the single-frequency characteristics of the output pulses and obtained the stability of the center frequency of the pulses. Figures 4(a) and 4(b) show a single-shot beat note signal and its fast Fourier transform (FFT) at the PRR of 300 Hz. The pulse spectrum width of Gaussian fitting

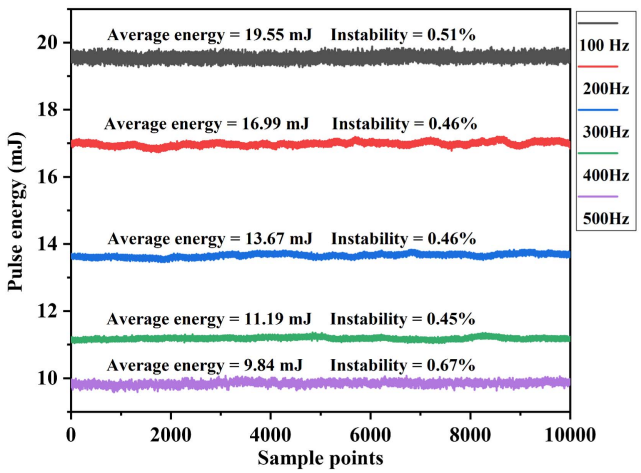

Fig. 3. Pulse energies at different PRRs of 100 Hz, 200 Hz, 300 Hz, 400 Hz, and 500 Hz.

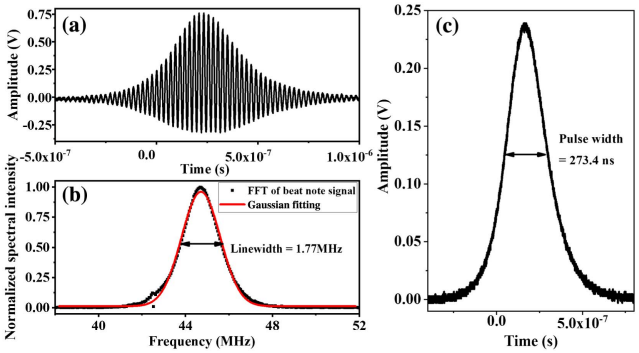

Fig. 4. (a) Single-shot beat note signal and (b) its FFT at the PRR of 300 Hz. (c) Single-frequency pulse waveform diagram.

is 1.77 MHz. Figure 4(c) shows a single-frequency pulse with a pulse width of 273.4 ns. The smooth pulse shape and perfect beat signal illustrate the single-frequency characteristic of the pulsed laser.

A 400 MS/s sampling rate data acquisition card was used to record the beat note signals, and we obtained the center frequency of the beat note signals by the FFT algorithm. As shown in Fig. 5, 10,000 center frequencies of the beat note signals and their distributions at each PRR from 100 Hz to 500 Hz were recorded. The standard deviations of the central frequencies at different PRRs from 100 Hz to 500 Hz are 82.72 kHz, 95.18 kHz, 115.32 kHz, 130.52 kHz, and 134.44 kHz, respectively. All center frequencies of the beat note signals follow the normal distribution nicely, which indicates that the unstable factors of pulse frequency are mainly random events. In the injection-seeding technique, the longitudinal mode closest to the seed's frequency is preferentially oscillated, and the other

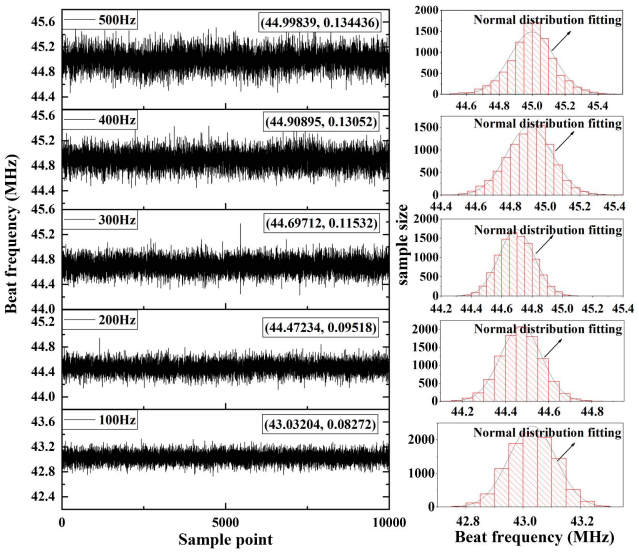

Fig. 5. Recorded center frequencies of the beat note signals (left) and their distributions (right) at different pulse repetition frequencies of 100 Hz, 200 Hz, 300 Hz, 400 Hz, and 500 Hz.

longitudinal modes are suppressed, resulting in a single-frequency pulse. Because the effective cavity lengths are different at different PRRs, which are caused by the thermal effect, the center frequencies of the beat note signal at different PRRs are also different.

Compared with the standard deviation, which is only convergent for white noise[26], Allan deviation is convergent for most types of noises, so it is more suitable to describe frequency stability in the time domain. In the measurement time t, the Allan variance of N ($N = t/\mathrm{PRR}$) pulse frequencies is defined as

$$\sigma_\nu^2(\tau) = \frac{1}{2}\langle(\nu_{i+1} - \nu_i)^2\rangle_\tau, \tag{7}$$

where ν_i is the mean value over a time interval of $\tau \le t/2$, ν_{i+1} is the mean value of the followed time interval of the same duration, and $\langle \ldots \rangle$ denotes the arithmetic mean. Figure 6 shows the Allan deviations of the beat note center frequencies at different PRRs as a function of time interval τ. We can notice that the Allan deviations at different PRRs are consistent with the Allan deviations of white noise ($\tau^{-1/2}$) in the overall trend, and the Allan deviations are almost all less than 100 kHz, which illustrate that the PDH injection-seeding method is a good way to improve the frequency stability of the single-frequency pulses. For averaging time < 1 s, white noise is the main factor affecting frequency stability. Because of others types of noise processes, the Allan deviations have large fluctuations for averaging time of more than 1 s. This indicates that the pulse accumulation time of about 1 s is suitable for lidar application.

The beam quality of the single-frequency pulses was detected by a beam profiling camera (Pyrocam IIIHR, Ophir Optronics Solutions Ltd.). Figure 7 shows the change of beam diameter with relative position at the PRR of 300 Hz, where the beam is focused by a convex lens with a focal length of 500 mm. Fitting the beam widths by a hyperbola line, the M^2 factors are calculated to be 1.24 and 1.21 in the X and Y directions,

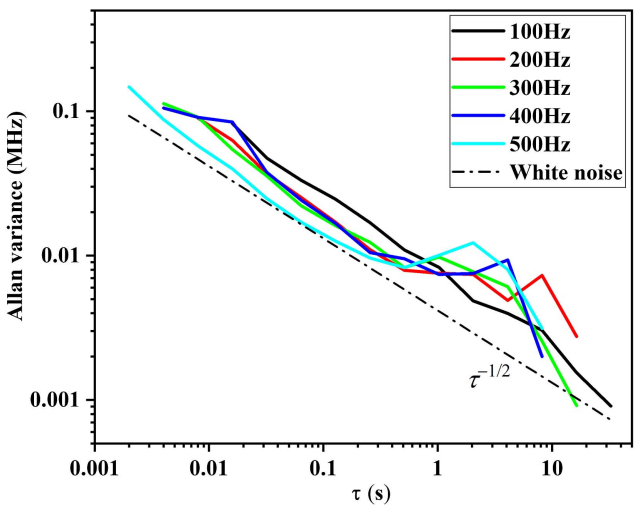

Fig. 6. Allan plot for pulse frequencies at different PRRs.

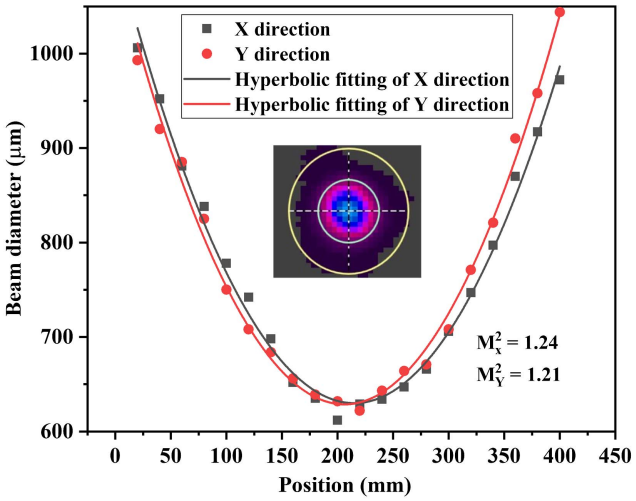

Fig. 7. Beam quality of the single-frequency pulses at the PRR of 300 Hz.

respectively. Thanks to the symmetrical pumping structure and the very small incident angle on the concave mirrors M3 and M5, the output laser beam has almost no astigmatism.

5. Conclusion

The PDH scheme also has a good performance in the injection-seeded pulse domain that was demonstrated. The frequency stability of an injection-seeded single-frequency 1645 nm pulsed laser can be controlled close to 100 kHz. It may be a good technical verification for the future space-based lidars. The single-frequency pulse energy varies from 9.84 mJ to 19.55 mJ with a relative energy instability of approximately 0.5% at the PRR from 100 Hz to 500 Hz. The output pulses also have a beam quality with M^2 factors of 1.24 in the X direction and 1.21 in the Y direction, respectively. What is more, the influence of pulse frequency jitter on SNR and measurement accuracy of lidar was also analyzed.

Acknowledgement

This work was supported by the National Natural Science Foundation of China (No. 61627821) and the Program of State Key Laboratory of Quantum Optics and Quantum Optics Devices (No. KF202103).

References

1. V. Wulfmeyer, M. Randall, A. Brewer, and R. M. Hardesty, "2-μm Doppler lidar transmitter with high frequency stability and low chirp," Opt. Lett. **25**, 1228 (2000).
2. Y. Zhu, J. Yang, X. Chen, X. Zhu, J. Zhang, S. Li, Y. Sun, X. Hou, D. Bi, L. Bu, Y. Zhang, J. Liu, and W. Chen, "Airborne validation experiment of 1.57-μm double-pulse IPDA LIDAR for atmospheric carbon dioxide measurement," Remote Sens. **12**, 1999 (2020).
3. N. Cezard, S. Le Mehaute, J. Le Gouet, M. Valla, D. Goular, D. Fleury, C. Planchat, and A. Dolfi-Bouteyre, "Performance assessment of a coherent DIAL-Doppler fiber lidar at 1645 nm for remote sensing of methane and wind," Opt. Express **28**, 22345 (2020).
4. X. Zhu, J. Liu, D. Bi, J. Zhou, W. Diao, and W. Chen, "Development of all-solid coherent Doppler wind lidar," Chin. Opt. Lett. **10**, 012801 (2012).
5. W. Diao, X. Zhang, J. Liu, X. Zhu, Y. Liu, D. Bi, and W. Chen, "All fiber pulsed coherent lidar development for wind profiles measurements in boundary layers," Chin. Opt. Lett. **12**, 072801 (2014).
6. Z. Bu, S. Chen, Y. Zhang, H. Chen, X. Ge, and P. Guo, "Effect of laser pulse shape and duration on spectrum width of coherent LIDAR," Chin. Opt. Lett. **12**, S12801 (2014).
7. X. Sun, J. Liu, J. Zhou, and W. Chen, "Frequency stabilization of a single-frequency all-solid-state laser for Doppler wind lidar," Chin. Opt. Lett. **6**, 679 (2008).
8. J. Caron and Y. Durand, "Operating wavelengths optimization for a space-borne lidar measuring atmospheric CO_2," Appl. Opt. **48**, 5413 (2009).
9. F. Gibert, D. Edouart, C. Cénac, and F. Le Mounier, "2-μm high-power multiple-frequency single-mode *Q*-switched Ho:YLF laser for DIAL application," Appl. Phys. B **116**, 967 (2014).
10. P. Kucirek, A. Meissner, S. Nyga, J. Mertin, M. Höfer, and H.-D. Hoffmann, "A single-frequency Ho:YLF pulsed laser with frequency stability better than 500 kHz," Proc. SPIE **10082**, 100821K (2017).
11. O. Lux, D. Wernham, P. Bravetti, P. McGoldrick, O. Lecrenier, W. Riede, A. D'Ottavi, V. De Sanctis, M. Schillinger, J. Lochard, J. Marshall, C. Lemmerz, F. Weiler, L. Mondin, A. Ciapponi, T. Kanitz, A. Elfving, T. Parrinello, and O. Reitebuch, "High-power and frequency-stable ultraviolet laser performance in space for the wind lidar on Aeolus," Opt. Lett. **45**, 1443 (2020).
12. F. Shen, Z. Wang, Y. Xia, B. Wang, P. Zhuang, and C. Qiu, "Quad-Fabry–Perot etalon based Rayleigh Doppler lidar for 0.2-60 km altitude wind, temperature and aerosol accurate measurement," Optik **236**, 166668 (2021).
13. J. Du, Y. Sun, D. Chen, Y. Mu, M. Huang, Z. Yang, J. Liu, D. Bi, X. Hou, and W. Chen, "Frequency-stabilized laser system at 1572 nm for space-borne CO_2 detection LIDAR," Chin. Opt. Lett. **15**, 031401 (2017).
14. L. A. Rahn, "Feedback stabilization of an injection-seeded Nd:YAG laser," Appl. Opt. **24**, 940 (1985).
15. S. W. Henderson, E. H. Yuen, and E. S. Fry, "Fast resonance-detection technique for single-frequency operation of injection-seeded Nd:YAG lasers," Opt. Lett. **11**, 715 (1986).
16. Y. Zhang, C. Gao, Q. Wang, Q. Na, M. Zhang, M. Gao, and S. Huang, "1 kHz single-frequency, injection-seeded Er:YAG laser with an optical feedback," Chin. Opt. Lett. **17**, 031402 (2019).
17. C. E. Hamilton, "Single-frequency, injection-seeded Ti:sapphire ring laser with high temporal precision," Opt. Lett. **17**, 728 (1992).
18. A. Sträßer, T. Waltinger, and M. Ostermeyer, "Injection seeded frequency stabilized Nd:YAG ring oscillator following a Pound–Drever–Hall scheme," Appl. Opt. **46**, 8358 (2007).
19. M. Ostermeyer, T. Waltinger, and M. Gregor, "Frequency stabilization of a Q-switched Nd:YAG laser oscillator with stability better 300 kHz following an rf-sideband scheme," Opt. Commun. **282**, 3302 (2009).
20. F. Gibert, D. Edouart, C. Cénac, F. Le Mounier, and A. Dumas, "2-μm Ho emitter-based coherent DIAL for CO_2 profiling in the atmosphere," Opt. Lett. **40**, 3093 (2015).
21. C. Chen, Q. Wang, S. Huang, X. Zhang, K. Wang, M. Gao, and C. Gao, "Single-frequency *Q*-switched Er:YAG laser with high frequency and energy stability via the Pound–Drever–Hall locking method," Opt. Lett. **45**, 3745 (2020).
22. D. S. Zrnic, "Estimation of spectral moments for weather echoes," IEEE Trans. Geosci. Electron. **17**, 113 (1979).
23. R. Frehlich and M. Yadlowsky, "Performance of mean-frequency estimators for Doppler radar and lidar," J. Atmos. Ocean. Technol. **11**, 1217 (1994).
24. Y. Zheng, C. Gao, R. Wang, M. Gao, and Q. Ye, "Single frequency 1645 nm Er:YAG nonplanar ring oscillator resonantly pumped by a 1470 nm laser diode," Opt. Lett. **38**, 784 (2013).
25. C. Chen, Z. Li, X. Jin, and Y. Zheng, "Resonant photodetector for cavity- and phase-locking of squeezed state generation," Rev. Sci. Instrum **87**, 103114 (2016).
26. D. W. Allan, "Statistics of atomic frequency standards," Proc. IEEE **54**, 221 (1966).